Scott Lillard[1], Frank Gac[2], Mike Paciotti[2], Phil Ferguson[3], Gordon Willcutt[4], Greg Chandler[5], and Luke Daemen[3]

The Influence of High Energy Proton Irradiation on the Corrosion of Materials

Reference: R.S. Lillard, F. Gac, M. Paciotti, P. Ferguson, G. Willcutt, G. Chandler, and L.L. Daemen, "**The Influence of High Energy Proton Irradiation on the Corrosion of Materials**", *Effects of Radiation on Materials:20th International Symposium, ASTM STP 1405*, S.T.Rosinski, M.L. Grossbeck, T.R. Allen, and A.S. Kumar, Eds., American Society for Testing and Materials, West Conshonhocken, PA, 2000.

Abstract: This paper presents a summary of our current efforts to characterize the real-time corrosion rates of materials during 800 MeV proton radiation at currents up to 0.4 mA. Specially designed corrosion probes, which incorporated ceramic seals, were mounted in flow tubes on a water manifold that allowed samples to be directly exposed to the proton beam at the Los Alamos Neutron Science Center. The water system that supplied the manifold provided a means for controlling water chemistry, measuring dissolved hydrogen concentration, and measuring the effects of water radiolysis and water quality on corrosion rate. Real-time corrosion rates during proton irradiation increased with average proton beam current. In addition, for any given material type, a trend in corrosion rate with probe location relative to the beam centerline was observed. These results are discussed within the context of particle type, particle flux, and energy deposition.

Keywords: corrosion, proton irradiation, electrochemical impedance spectroscopy, particle flux, energy deposition, Alloy 718, type 316L stainless steel, aluminum alloy 6061, photons, neutrons, protons, EIS

Spallation neutron source target/blanket cooling loops present a unique combination of parameters that may effect the corrosion rates of metals, including high energy protons, high and low energy neutrons, gamma radiation, and water radiolysis products. In previous publications, Lillard and Butt have described a novel method for measuring the corrosion rate of materials in spallation neutron sources*[1, 2]*. Lillard measured the real-time corrosion rate of Alloy 718 with electrochemical impedance spectroscopy (EIS) during irradiation in an 800 MeV proton beam at the Los Alamos Neutron Science Center (LANSCE). In that work, the in-beam Alloy 718 samples were tested in a water system that provided a means for controlling water chemistry, measuring dissolved hydrogen

[1] Materials Corrosion and Environmental Effects Lab, Materials Science and Technology Division, MST-6, Los Alamos National Laboratory, Los Alamos, NM 87545.
[2] APT-TPO, Los Alamos National Laboratory, Los Alamos, NM 87545.
[3] LANSCE-12, Los Alamos National Laboratory, Los Alamos, NM 87545.
[4] TSA-10, Los Alamos National Laboratory, Los Alamos, NM 87545.
[5] Westinghouse Savannah River Company, Aiken, SC 29808.

concentration, and measuring the effects of water radiolysis and water quality on corrosion rate. It was shown that the real-time polarization resistance of Alloy 718 decreased from 1.7×10^3 ohm·m^2 in the absence of irradiation to 8.2 ohm·m^2 during proton irradiation at an average beam current of 0.4 mA*[3]*. Because the proton beam spot size was smaller than the sample, two methods for determing corrosion rate from polarization resistance were employed. The first method assumed that the distribution of corrosion was uniform across the entire probe surface. With this assumption, the corrosion rate for Alloy 718 was found to vary with average proton beam current from 0.041 μm/yr. at an average current of 0.001 mA to 3.1 μm/yr. at an average current of 0.40 mA. The second method used proton flux as a criterion for determining the area of highest damage. In the proton flux distribution model of corrosion, for an average beam current of 0.4 mA the corrosion rate for Alloy 718 on beam centerline (peak proton flux of 1.77×10^{18} p/m^2·s) was determined to be 60.9 μm/yr. The foundation for this flux model was based on thickness measurements from tungsten rods irradiated in a separate cooling water loop at LANSCE. In that work Sommer *et al.* found that the post irradiation thickness profiles of W rods, irradiated at a beam current of 1.0 mA for approximately two months, were Gaussian and corresponded to the Gaussian profile of the beam*[4]*. From these observations of W corrosion during proton irradiation a Gaussian distribution model for corrosion damage appeared to be justified.

Given the short irradiation time in the Lillard and Butt study (several months) and the low corrosion rates of Alloy 718, physical verification of the proton flux model was not possible (via post-irradiation thickness measurements of the probes). To verify the flux model, one would like to measure the real-time polarization resistance of a material as a function of radial distance from the proton beam centerline for each average beam current. The corrosion rate at any given position should be proportional to the Gaussian distribution proton current

$$\phi_o \, exp\left\{ -r^2 \Big/ 2\sigma^2 \right\} \tag{1}$$

where r is the radial distance from the proton beam center, σ is the Gaussian distribution of the flux and φ_o is given by

$$\phi_o = I_t \Big/ 2\pi\sigma^2 \tag{2}$$

and I_t is the beam current*[5]*.

In this paper, real-time corrosion rates as a function of average beam current and radial position from the proton beam centerline were measured with EIS for several engineering alloys proposed for spallation neutron target/blanket cooling loops. The probes used in this work were similar in design to those in previous studies. The corrosion data were analyzed within the context of particle flux (proton, neutron, and photon), as well as particle energy deposition (thermal hydraulics).

Experimental

The In-beam Corrosion Loop

All experiments were conducted at the A6 Target Station of LANSCE. A detailed description as well as diagrams of the beam line at A6, the corrosion water loop, and

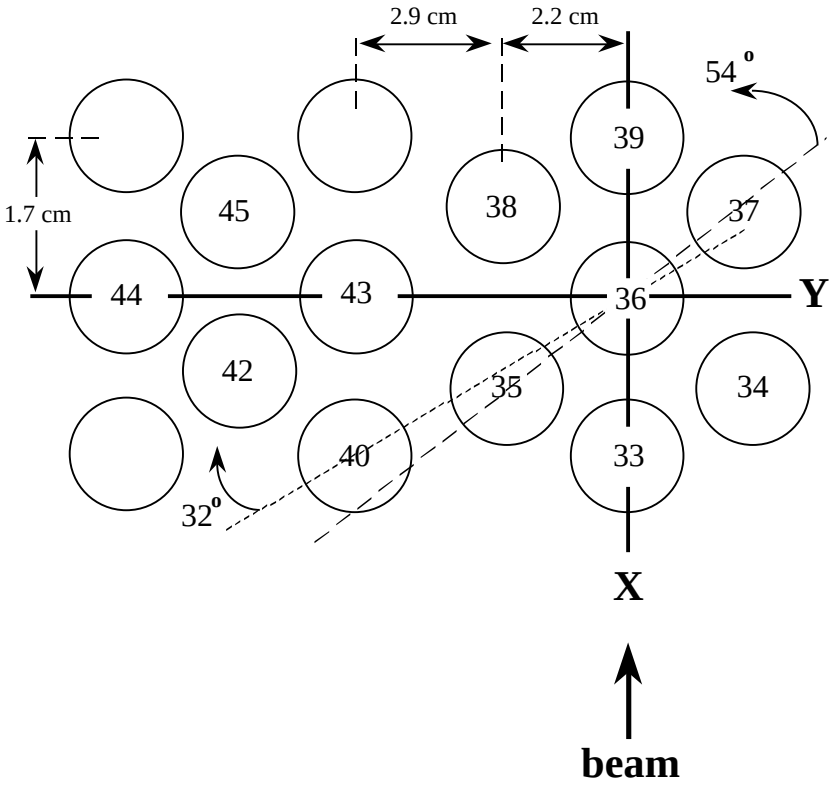

Figure 1 - *A perspective of the tube array irradiated during the FY '99 irradiation at the LANSCE A6 target station from the front, top-down. The path of the proton beam was parallel to the X axis at Y=0. Here we have defined the center of tube #36 as (0,0). Each numbered tube contained a corrosion probe. Alloy 718: 33, 39, and 45; SS 316L: 35, 36, 38, and 40; Al6061: 42, 43, and 44.*

probe design have been presented elsewhere*[2]*. Briefly, the corrosion water loop consisted of a water pumping system that supplied a manifold, which held the corrosion samples in-beam and provided water cooling of the samples. With the exception of the individual corrosion samples, the system was fabricated entirely of type 304 stainless steel (SS). To measure real-time in-beam corrosion rates, it was necessary to isolate electrically the corrosion samples from the stainless steel plumbing system. Conventionally, this can be accomplished with metal-to-glass seals. To overcome the problems associated with metal-to-glass seals in a proton environment, a corrosion probe that employed ceramic to metal seals was employed*[1-3]*. The only significant design difference as compared to previous investigations was the configuration of the water manifold. In this investigation the water manifold (Fig. 1) consisted of fifteen, 15 cm long by 1.73 cm inside diameter flow tubes arranged in close-packed arrays. Each tube contained either an in-beam corrosion probe that was 15.9 cm in length by 1.27 cm in outside diameter or a flow restrictor (unnumbered tubes in Fig. 1). With respect to water flow, tubes 33-39 were in parallel with one another and in series with tubes 40-45 (which were also in parallel with on another). The manifold was welded to the bottom of a 3.4 m supporting insert that not only supported the weight of the manifold but also provided the necessary conduits for electrical and water connections. Thermocouples attached to the front of the manifold verified the position, size, and shape of the proton beam.

Sample Preparation and Water Quality

To provide a fresh metal surface for electrochemical characterization, all samples were ground to 400 p SiC paper. After grinding, the samples were degreased in an ultrasonic bath of acetone. Degreasing was followed by successive sonications in ethanol and de-ionized water. Prior to placing the probes in the water system, the interior of the water system, which included all piping, tanks, and pumps, was rinsed with a mixture of water and ethanol. The water system was then filled with approximately 230 L of deionized (DI) water, operated for several hours, and then flushed. This DI rinse was repeated three times before the final system fill with DI water. The water resistivity varied between 1 $x10^6$ ohm·cm (initial) and $8x10^4$ ohm·cm (after several weeks of operation). Nominally, the system operated at an inlet water temperature between 18^o C (beam off) and 24^o C (0.340 mA), a pressure of 1.02 MPa, and a total flow rate of 0.91 L/s. This resulted in a flow rate of 0.13 L/s for the in-beam probes (tubes 33-39) and 0.11 L/s for the near-beam probes (tubes 40-45), and a water velocity of 1.21 m/s. The resulting Reynolds numbers for the in-beam and near-beam tubes were 6214 and 5434 respectively (calculated at 25^o C). In an attempt to mitigate the formation of water radiolysis products such as H_2O_2 *[6-9]*, the system was operated with a dissolved hydrogen concentration of approximately 0.40 mole/m^3. This was accomplished by continuously bubbling 6% H_2 - 94% Ar gas into the system's reservoir tank. A thorough discussion of the effects of water radiolysis on corrosion and mitigation methodology has been presented elsewhere*[10]*.

Proton Beam Characteristics

The flux of the incident proton beam had a Gaussian distribution of $2\sigma \approx 3.5$ cm. The energy of this particle beam was 800 MeV. The pulsed beam was characterized by a gate length (macropulse), a macropulse repetition rate, and a fixed peak current (Table 1). Average proton beam currents were controlled by varying the gate length as well as the repetition rate. Nominally, the average proton beam currents were varied between 0.01 and 0.4 mA. Therefore, the irradiation source was a complex pulsed beam and each of its components may play a disproportionate role in the measured corrosion rate. Thus, in extrapolating these results, the beam characteristics must be considered.

Table 1 *Proton beam parameters for corrosion data*.

Average Current (mA)	Peak Current (mA)	Repetition Rate (Hz)	Gate Length (μs)	Duty Cycle (milli-cycles)
0.010	16	3	200	0.600
0.036	16	10	200	2.00
0.10	16	10	625	6.25
0.34	16	36	625	21.6

Electrochemical Measurements

EIS*[11-14]* was used to measure the polarization resistance of each sample as a function of average beam current and irradiation time. To maximize the signal-to-noise ratio, measurements were conducted with a 30 mV peak-to-peak sinusoidal voltage

perturbation[6] over the frequency range of 0.005 - 1000 Hz. No applied dc potential was employed; that is, all measurements were conducted at the open circuit potential (OCP). To eliminate the effects of ground loops, a floating ground EIS system was used. In these measurements, the traditional three electrode set-up was used. Here the 304 SS water system acted as the counter electrode. Because a traditional reference electrode was not capable of withstanding the proton / neutron flux at the manifold, one of the in-beam corrosion probes was used as a reference.

All electrochemical measurements were conducted while the proton beam was on.

Radiation Transport Calculations

In an attempt to correlate corrosion rate directly with particle flux, radiation transport calculations, including energy deposition and particle flux calculations, were completed using MCNPX. MCNPX*[15, 16]* is the result of the merger of the Monte Carlo transport codes LAHET*[17]* and MCNP*[18]*. MCNPX™ is a general particle transport code that spans a broad range of particle energies, from sub-MeV to multi-GeV. Charged particles, light ions, and high-energy neutrons use the physics modules of LAHET™ to simulate particle transport and nuclear interactions. As with MCNP™, transport and nuclear interactions of photons and low-energy neutrons use evaluated nuclear data. MCNPX can be used to model arbitrarily complex geometries and multiple material compositions. Uncertainties in MCNPX energy deposition calculations at 800 MeV for in-beam and near-beam samples are generally expected to be within 20% as shown by Corzine, *et al.[19, 20],* and by Beard and Belyakov-Bodin *[21]*.

Particle flux tallies were completed using the standard flux averaged over the volume of a cell or the new mesh tally in MCNPX for neutral particles. For charged particles, fluxes were calculated on the surface of a cell. Uncertainties in the particle fluxes are more difficult to quantify. Although the secondary particle source is probably well predicted as evidenced by the work of Morgan, et al.*[22]*, there may be errors in the prediction of the angular distribution leading to increasing uncertainty in the calculated particle fluxes as a function of distance from the proton beam centerline. As a guide, an uncertainty of approximately 20% can be assumed for the particle fluxes with larger errors possible in the outer regions. In general, the relative comparisons of the calculations (one calculation vs. another) are more accurate than the absolute comparison of a single calculation.

In addition to the surrounding A6 experiment region, the Monte Carlo model included each probe, the surrounding water layer, and the outer SS 304 tube explicitly. The corrosion probes were assumed to be hollow cylinders as opposed to modeling the rounded ends. Energy deposition calculations were performed along the probe in 1 cm long cells to provide input for temperature calculations as a function of position to allow an analysis of the axial heat flow. In addition, detailed mesh tallies (~3 mm grid spacing) were completed for multiple sections of the geometry with energy deposition separated by particle type. Particle flux tallies were also performed as detailed mesh tallies, as well as averaged over the entire length of the probe. The probe length averages are believed to correspond better with the measurements because the measurements include effects along the length of the probe.

Particle flux and the resulting energy deposition was also used to calculate probe surface temperature (peak and average). For each location, the probe and tube surface

---

[6] Although a 30 mV perturbation is somewhat higher than that typically used in EIS measurements, for metals undergoing passive dissolution the effect of an applied anodic voltage is to thicken the passive film. However this increase is small. Therefore, no appreciable effect of the 30 mV signal sample is anticipated.

™ MCNPX, MCNP, and LAHET are registered trademarks of the University of California.

temperatures were determined using the local water temperature and material power densities from the radiation transport calculations described above. The probe water side surface temperature was determined by adding the film temperature drop to the bulk water temperature, where the film temperature drop was determined by dividing the heat flux by the heat transfer coefficient. The heat flux was caused by the power deposited in the probe wall with the inside of the probe being adiabatic. The surface temperature for the inner side of the probe was determined by adding the temperature increase through the probe wall to the outer surface temperature, where the temperature increase through the wall was obtained from a conduction solution with internal heat generation in the hollow cylindrical wall. A similar calculation is done for the tube wall, except the heat flux was removed from the inner surface and the outer surface was adiabatic. These calculations use one-dimensional assumptions in the radial direction. A separate two-dimensional calculation was done to determine the impact of axial conduction along the probe, and it was shown to be very small. A separate three-dimensional model was used to calculate the temperatures of the thermocouples attached on the outside of the flow tubes. An approximation to this model was then incorporated in the spreadsheet model to calculate the thermocouple temperatures along with the probe and tube wall surface temperatures.

Results

Typical EIS data from a SS 316L in-beam corrosion probe are presented in Fig. 2 in the form of Bode magnitude and phase plots (tube 35, 0.036 mA avg. beam current). The magnitude of the impedance has been normalized for area by multiplying |Z| by the total sample area (approximately 6.34×10^{-3} m^2). To obtain polarization resistance (R_{pol}) from the data, complex non-linear least squares (CNLS) fitting of the data was employed. To model the data several electrical equivalent circuits (EC) were used. For SS 316L and Al6061 the electrical equivalent circuit presented in Fig. 3 was used (Warburg model*[23, 24]*) while for Alloy 718 a simplified Randles circuit was used*[3]*. In the Warburg model R_{pol} is the polarization resistance, C_{dl} is the capacitance associated with the double layer, Z_W is a diffusion (Warburg) impedance, and R_{sol} is the geometric solution resistance between the sample and the water system. A CNLS fit of the in-beam data to this EC is also presented in Fig. 2. As seen in this figure, good agreement between the model and the data exists.

From R_{pol} the corrosion rate, CR in μm/yr., was determined from the well known relationship*[25]*

$$CR = \frac{327.6\left(26/R_{pol}\right)(EW)}{\rho} \qquad (3)$$

where ρ is the density of the material in kg/m^3, the units conversion constant 327.6 has units of (kg·μm)/(m·mA·yr.), and EW is the equivalent weight (dimensionless). The constant 26 has units of mV and assumes Tafel slopes of 0.12 V/decade. The error

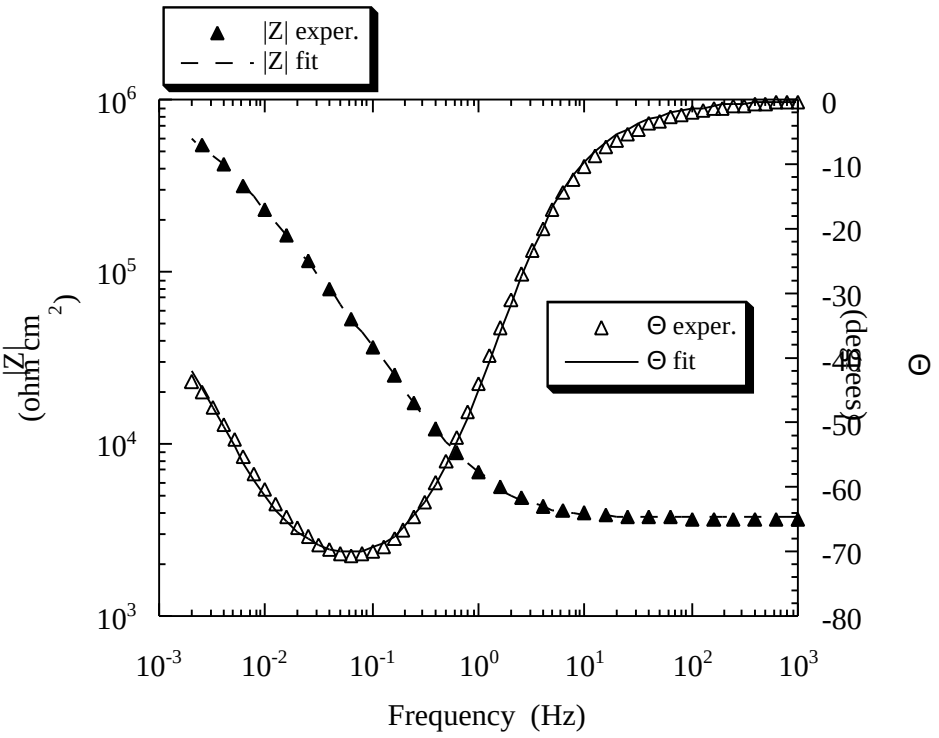

Figure 2 - *Bode magnitude and phase plots for SS 316L in tube 35 during proton irradiation at 0.036 mA. The CNLS fit of the data to the Warburg model in Fig. 3 is also presented. For clarity, not all experimental data are shown.*

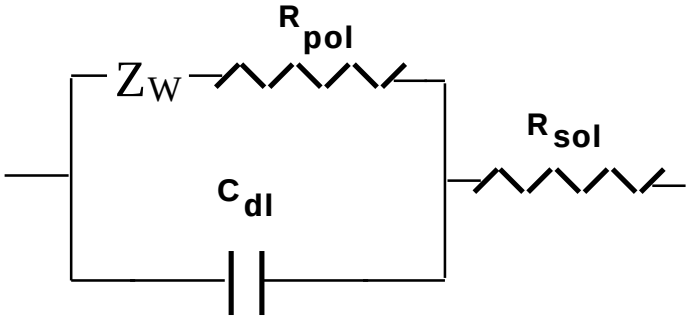

Figure 3 - *Warburg equivalent circuit used to model the SS 316L EIS data. Where: R_{pol} is the polarization resistance, R_{sol} is the geometric solution resistance, C_{dl} is the double layer capacitance, and Z_W is a Warburg type impedance (diffusion impedance).*

associated with this assumption is small and has been addressed elsewhere*[13]*. A plot of uniform corrosion rate as a function of proton beam current is presented in Figs. 4a, 4b, and 4c for Alloy 718, SS 316L, and Al6061 respectively. These plots assume that corrosion occurred uniformly across the entire sample surface. Corrosion rate increased as a function of average beam current for all materials. By plotting the data on a log-log scale these relationships can be expressed by*[3]*

$$log(CR) = \alpha + \beta\, log(BC) \qquad (4)$$

where BC is the average proton beam current in mA and α and β are constants and depend on tube location and material type respectively. For any single material β was relatively independent of sample location where as α decreased with distance from the beam centerline for any given material (Table 2). Thus β appears to be related to material type while α is related to sample location.

Table 2 - Variables from curve fit analysis of Equation 4 to corrosion rate data and the corresponding correlation coefficient (r).

tube #	α	β	r
SS 316L: 35	0.99	0.97	0.998
36	1.2	0.95	0.998
38	1.1	0.92	0.999
40	0.48	0.76	0.987
Al6061: 42	1.1	1.4	0.999
43	0.98	1.4	0.989
44	0.35	1.2	0.979
718: 33	0.95	1.0	0.994
39	1.1	1.0	0.992

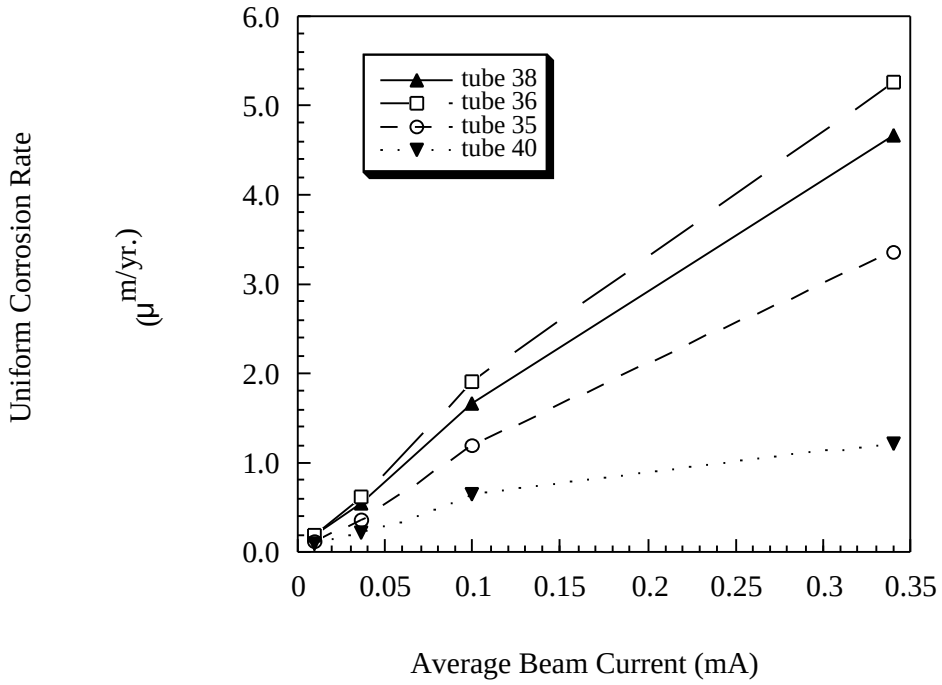

Figure 4a - *Corrosion rate as a function of average beam current for the SS 316L probes.*

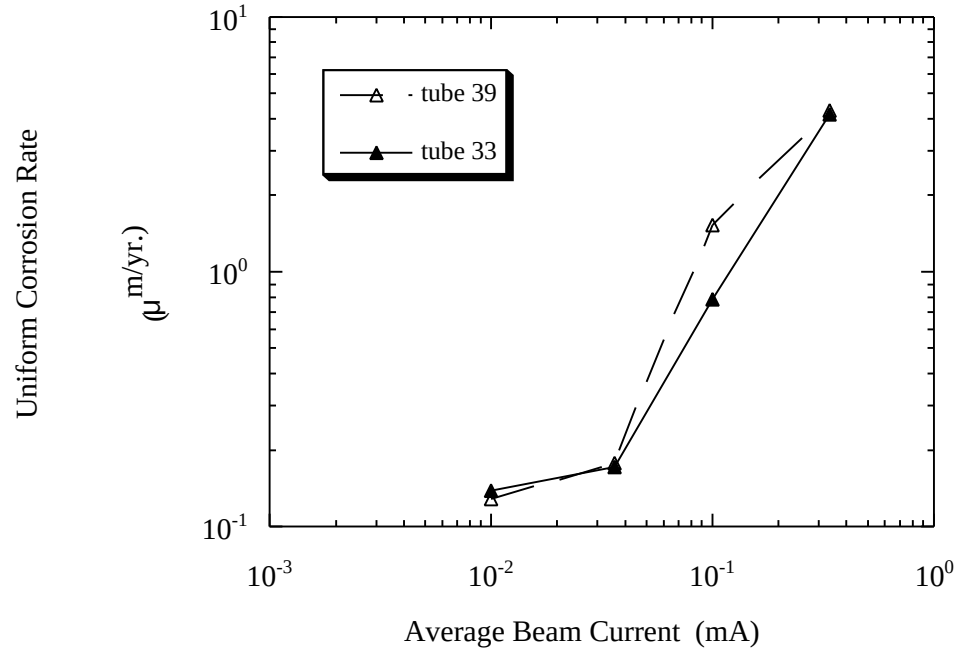

Figure 4b - *Corrosion rate as a function of average beam current for the Alloy 718 probes at the beam centerline.*

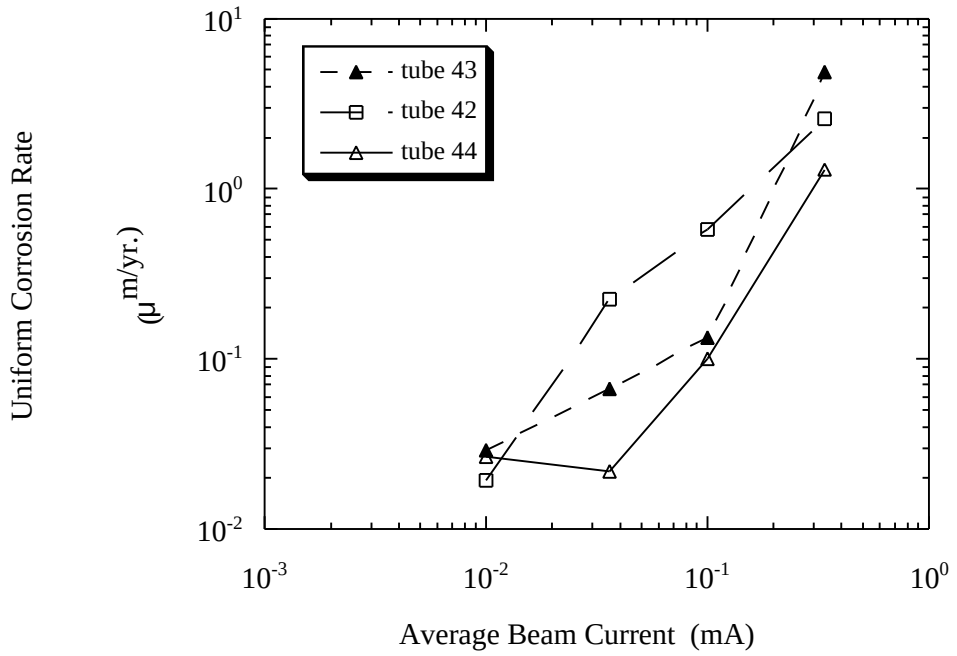

Figure 4c - *Corrosion rate as a function of beam current for the Al6061 probes.*

Discussion

Although the plots in Figs. 4a to 4c assume uniform corrosion across the entire sample surface, this assumption may not be valid as analysis of these figures reveals several trends in corrosion rate with probe location. The most notable trends with position were observed in the SS 316L data where corrosion rate increased in the order (by tube number) 40 < 35 < 38 < 36. It is apparent that the trend in corrosion rate with sample location is not a simple function of radial distance from the beam as predicted by Eq. 1 and previously modeled*[3]*. For example, although tubes 35 and 38 are equidistant from the beam centerline (tube 36) the corrosion rate of SS 316L sample in tube 38 was consistently greater than the corrosion rate of the sample in tube 35. Several potential explanations for the observed differences in corrosion rate between sample location include changes in the passive film and charging at the double layer (the solution/metal interface) owing to interactions with ionizing radiation, water radiolysis, and temperature. To evaluate these mechanisms, a thorough analysis of particle flux from radiation transport calculations, and energy deposition (as it relates to sample temperature) was necessary.

Sample results from the radiation transport calculations are presented in Table 3 for the SS 316L specimens. A direct correlation between both neutron and photon flux with corrosion rate was observed. For neutrons and photons, the flux increased in the order (by tube number) 40 < 35 < 38 < 36. In comparison, the SS 316 L corrosion rate also increased in the order 40 < 35 < 38 < 36. However, as seen in Table 3 proton flux did not predict the relationship between corrosion rate and sample location. Other differences between protons and neutrons and photons also exist. For example, the ratio of the maximum to minimum proton flux was 21 (tube 36 : tube 40), while the maximum to

Table 3 - *Results from radiation transport calculations for tubes containing SS 316L samples. Flux was averaged over the tube length and summed for all particle energies.*

tube #	proton flux $p/m^2 \cdot s \cdot mA$	neutron flux $n/m^2 \cdot p$	photon flux $g/m^2 \cdot p$
35	72.7	38.0	35.2
36	127	52.7	46.2
38	70.9	43.8	37.3
40	6.0	13.5	13.2

minimum photon flux was 3.5. The ratio of the maximum to minimum corrosion rate for SS 316L was 4.3 (tube 36 : tube 40; 0.34 mA beam current). Currently, we are examining these relationships between particle flux and corrosion rate for all sample materials and probe locations. In addition, we are also evaluating energy deposition by particle type both in the sample and the water annulus surrounding the sample as potential explanations for the observed changes in corrosion rate with location and beam current.

Sample results from the thermal hydraulic calculations are presented in Table 4 for SS 316L. Similar trends in measured and calculated TC readings were observed, however, the calculated temperatures were consistently higher than the measured values. This difference likely owed to assumptions made in the modeling of the TC/tube braze. The model assumed that the braze was uniform along the TC shield to the tip of the TC. In practice, the brazes extended beyond the tip and gaps existed between the shield and tube where the braze did not wet. Calculated peak probe water-side surface temperatures were as high as 112° C for the probe on beam centerline for the maximum beam current. At the minimum beam current (0.01 mA) the temperature of this probe was close to water temperature. The measured and calculated temperature trends increased in the same order as proton flux 40 < 38 < 35 < 36. This is not surprising as the relative probe temperatures reflect the differences in total energy deposition which is dominated by proton flux. However, the trend in temperature did not correlate with the measured trends in corrosion rate for SS 316L. In addition, for passive metals the increase in corrosion rate as a function of temperature below 100^{o}C is small (closed systems). For example, for Alloy 718, it has been shown that a 50^{o}C increase in sample temperature produced a 33% increase in corrosion rate*[3]*. Although the change in corrosion rate due to an increase in temperature is small relative to the changes in corrosion rate measured during proton irradiation, the measured corrosion rate must be considered as the sum of the increase due to changes in materials properties (oxide film and double layer changes) as well as temperature.

Table 4 - *Thermocouple (TC) and probe temperatures calculated at a beam current 0.342 mA (SS 316L only, water-side, peak temp). Actual TC temperatures measured at a beam current of 0.34 mA are also presented.*

tube #	TC, Measured ^{o}C	TC, Calculated ^{o}C	Calculated Probe Temperature, ^{o}C
35	48.1	64.2	81.7
36	66.9	94.6	112.2
38	53.4	63.9	79.2
40	33.8	30.8	28.9

Conclusions

Corrosion rate increased with average proton beam current for all materials examined consistent with previous studies on Alloy 718 during proton irradiation. Fitting of the data to a log - log relationship gave a slope that was related to material type and intercept that was proportional to sample location relative to the beam centerline. Transport calculations revealed that the flux of neutrons and/or photons appears to correlate with corrosion rate. Proton flux data from these results did not predict the observed trend in corrosion rate as a function of sample location. Further, the ratio of maximum to minimum proton flux was much larger than the ratio of maximum to minimum corrosion rate. Probe surface temperature calculations based on total energy deposition did not predict the observed trend in corrosion rate as a function of sample location. However, it was concluded that the observed trends in corrosion rate with beam current had a component that was related to sample temperature.

Acknowledgment

Work on this project was performed by the University of California under the auspices of the United States Department of Energy contract W7405-ENG36. The authors would like to thank Laurie Waters and the continued support of the APT Project Office; Walt Sommer, Stuart Maloy, and Mike James for helpful discussions; Richard Werbeck, Michael Baumgartner, and the rest of the LANSCE-7 group for their engineering expertise; R.G. Stone and R.E. Loehman (Sandia National Lab) for manufacturing the corrosion probes. In memory of Russ Kidman (LANL).

References

[1] Lillard, R. S. and Butt, D. P., *Journal of Materials*, vol. 50, 1998, pp. 56.

[2] Lillard, R. S. and Butt, D. P., *Materials Characterization*, vol. 43, 1999, pp. 135.

[3] Lillard, R. S., Willcutt, G. J., Pile, D. L., and Butt, D. P., *Journal of Nuclear Materials*, vol. 277, 2000, pp. 250.

[4] Sommer, W., Maloy, S., and Zaslawsky, M., "Proton Beam Effects on Tungsten Rods, Surface Cooled by Water," presented at 2nd International Workshop on Spallation Materials Technology, Ancona, Italy, 1997, pp. 215.

[5] Sommer, W. F., "APT Materials Safety Experiments Technical Report," Los Alamos National Laboratory, Los Alamos LAUR-93-2850, August 1993.

[6] Indig, M. E. and Weber, J. E., "Mitigation of Stress Corrosion Cracking in an Operating BWR," in Corrosion/83, NACE, Houston, TX, 1983, paper no. 124.

[7] Fox, M., "Water Chemistry and Corrosion in BWRs," in Corrosion/83, NACE, Houston, TX, 1983, paper no. 123.

[8] Fox, M. J., "A Review of Boiling Water Reactor Chemistry: Science, Technology, and Performance," Argonne National Laboratory for the US Nuclear Regulatory Commission NUREG/CR-5115 ANL-88-42, February 1989.

[9] Lin, C. C., Cowan, R. L., and Pathania, R. S., "Evaluation of ECP Measurements in BWR's During HWC Tests," in Corrosion/93, NACE, Houston, TX, 1993, paper no. 619.

[10] Lillard, R. S., Pile, D. L., and Butt, D. P., *Journal of Nuclear Materials*, vol. 278, 2000, pp. 277.

[11] MacDonald, D. D., "Electrochemical Impedance Techniques in Corrosion Science," in *Electrochemical Corrosion Testing, ASTM STP 727*, F. Mansfeld and U. Bertocci, Eds. ASTM, Philadelphia, 1981, pp. 110.

[12] MacDonald, J. R., *Impedance Spectroscopy*. Wiley Publishing, New York, 1987.

[13] Mansfeld, F., "Polarization Measurements," in *Electrochemical Techniques*, R. Baboian, Ed. NACE, Houston, 1986, pp. 67.

[14] Sluyters-Renbach, M. and Sluyters, J. H., *Electroanalytical Chemistry*, vol. 4, no. 1, 1970, pp. 1.

[15] Hughes, H. G., "The MCNPTM/LAHET™ Merger Project," in *Proceedings of the Topical Meeting on Nuclear Applications of Accelerator Technology*, Albuquerque, NM, November 16-20, 1997, pp. 213.

[16] Hughes, H. G., "Recent Developments in MCNPX™," in *Second International Topical Meeting on Nuclear Applications of Accelerator Technology*, Gatlinburg, Tennessee, September 20-23, 1998, pp. 281.

[17] Prael, R. E. and Lichtenstein, H., "User Guide to LCS: The LAHET Code System," Los Alamos National Laboratory LA-UR-89-3014, September, 1989.

[18] Briesmeister, J. F., "MCNP - A General Monte Carlo N-Particle Transport Code," Los Alamos National Laboratory LA-12625-M, Version B, March, 1997.

[19] Corzine, R. K., "MCNPX Benchmark of In-beam Proton Energy Deposition," Los Alamos National Laboratory, Los Alamos, New Mexico LAUR-00-0138, January 2000.

[20] Corzine, R. K., "MCNPX Benchmark of Out-of-Beam Energy Deposition in LiAl," Los Alamos National Laboratory, Los Alamos, New Mexico LAUR-00-0711, February 2000.

[21] Beard, C. A. and Belyakov-Bodin, V. I., *NS&E*, vol. 199, 1995, pp. 87-96.

[22] Morgan, G., "LANL Sunnyside Experiment: Study of Neutron Production in Accelerator-Driven Targets," in *Proceedings of the International Conference on Accelerator-Driven Transmutation Technologies and Applications*, vol. 346. AIP Conference Proceedings, 1994, pp. 682-689.

[23] Armstrong, R. D., Bell, M. F., and Metcalfe, A. A., *Electrochemistry - Specialist Periodical Reports*, vol. 6, 1978, pp. 98.

[24] MacDonald, D. D., "Theoretical Analysis of Electrochemical Impedance," in Corrosion/87, NACE, Houston, TX, 1987, paper no. 479.

[25] Fontana, M. G., *Corrosion Engineering*. McGraw-Hill, New York, 1986.